

A symmetry-based protocol to benchmark quantum simulation of many-body physics

Aditya Prakash^{1,2} Bharath Hebbe Madhusudhana³

¹*National Institute of Science Education and Research Bhubaneswar, Jatni, Odisha 752050, India*

²*Homi Bhabha National Institute, Training School Complex, Anushakti Nagar, Mumbai 400094, India*

³*MPA-Quantum, Los Alamos National Laboratory, Los Alamos, NM-87544, United States*

Quantum simulation of many-body systems, particularly using ultracold atoms and trapped ions, presents a unique form of quantum control — it is a direct implementation of a multi-qubit gate generated by the Hamiltonian. As a consequence, it also faces a unique challenge in terms of benchmarking, because the well-established gate benchmarking techniques are unsuitable for this form of quantum control. Here we show that the symmetries of the target many-body Hamiltonian can be used to benchmark and even characterize experimental errors in the quantum simulation. We consider two forms of errors: (i) unitary errors arising out of systematic errors in the applied Hamiltonian and (ii) canonical non-Markovian errors arising out of random shot-to-shot fluctuations in the applied Hamiltonian. We show that the dynamics of the expectation value of the target Hamiltonian itself, which is ideally constant in time, can be used to characterize these errors. In the presence of errors, the expectation value of the target Hamiltonian shows a characteristic thermalization dynamics, when it satisfies the operator thermalization hypothesis (OTH). That is, an oscillation in the short time followed by relaxation to a steady-state value in the long time limit. We show that while the steady-state value can be used to characterize the coherent errors, the amplitude of the oscillations can be used to estimate the non-Markovian errors. We develop two experimental protocols to characterize the unitary errors based on these results, one of which requires single-qubit addressing and the other one doesn't. We also develop a protocol to detect and partially characterize non-Markovian errors.

I. INTRODUCTION

In quantum simulation, the properties of a quantum many-body Hamiltonian are simulated using a highly controllable quantum system. This includes simulating ground-state properties via adiabatic sweeps and simulating time dynamics using a quench. Both of these have been demonstrated in various platforms including ultracold atoms in an optical lattice [1, 2] suitable for simulating Fermi/Bose-Hubbard model and its variants, ion traps [3–5] and Rydberg atoms trapped in optical tweezers [6, 7], well-suited to simulate variants of Ising models. Both the adiabatic sweep and quench dynamics produce a multi-qubit gate — an entangling quantum gate acting on a large quantum system, usually the set of all qubits. Such multi-qubit gates can expand the gate-set of quantum control in general and can be used to develop digital-analog quantum computers [8, 9]. They can also be used, in a case of practical quantum advantage, to benchmark new ansatz-based efficient classical algorithms to solve for the properties of the same Hamiltonians [10]. A very important limitation to all of these applications is the experimental errors incurred in the simulation, which need to be benchmarked [11].

One and two-qubit gates can be benchmarked via a process tomography [12]. At the device level, one can use randomized benchmarking and its variants [13–16]. However, neither of these are suited for benchmarking quantum simulation of a particular many-body Hamiltonian. Cross-platform benchmarking is a possible solution, where the simulation of the same Hamiltonian, done independently on two different platforms, are compared to estimate the total error. The key aspect here

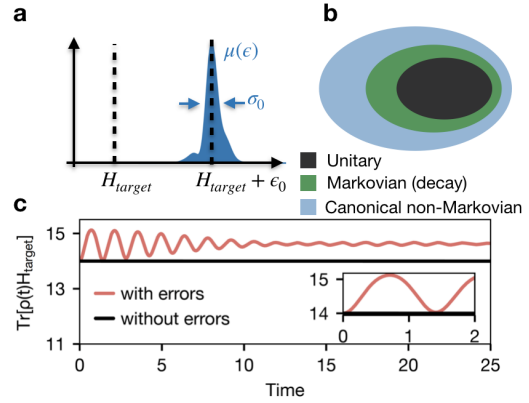


Figure 1. Errors in quantum simulation: **a.** Model of realistic experimental errors in the implementation of a target Hamiltonian H_{target} . Errors, ϵ in the implemented Hamiltonian maybe modelled by a distribution $\mu(\epsilon)$ in the space of Hamiltonians. It may have a systematic part, i.e., a non-zero average ϵ_0 and a random part, i.e., a non-vanishing waist σ_0 . **b.** Classification of experimental errors. The systematic part ϵ_0 causes a unitary error (black), i.e., the unitary implemented is different from the target. The shot-to-shot fluctuations cause canonical non-Markovian errors, i.e., the map implemented is non-unitary and non-markovian (blue). Any decay modelled by a Lindblad master equation causes Markovian errors (green). **c.** The dynamics of H_{target} as an observable with and without errors. Without errors, it is trivially constant; with errors, it shows short-lived oscillations which relax the the long-time limit. The amplitude of the oscillations can be used to estimate the canonical non-Markovian error, while the steady-state value can be used to characterize the unitary errors.

is to estimate the fidelity between quantum states of two different experimental systems, for which, the state-of-the-art protocols require an exponentially large number of measurements [17, 18].

Hamiltonian learning is another technique that can be used to benchmark many-body quantum simulations. Here, the target Hamiltonian is compared with the experimental Hamiltonian, determined via Hamiltonian tomography. The latter can be done efficiently for local Hamiltonians by using thermal state [19] or quench dynamics [20–22]. However, these protocols assume that the dynamics are unitary, ignoring coupling to external baths and non-Markovian errors. An alternative approach is to use random matrix theory. A state produced after a long time evolution under a typical many-body Hamiltonian has universal statistical properties, which maybe violated if there are experimental errors. For a given single-qubit subsystem, the first moment of the set of states it can collapse to form the many-body state is precisely its reduced density matrix. Interestingly, the higher moments encompass universal statistical properties, which can be characterized by the k -designs that emerge. This was shown theoretically [23] and also observed experimentally [24]. Therefore, one can develop a benchmark that would characterize errors that deviate the dynamics from ergodicity. This approach has been used to solve the metrological challenge mentioned above, by developing a sample efficient benchmarking scheme [25]. However, this approach still requires an exact classical simulation of the dynamics, i.e., the computational challenge is unaddressed. More recently, an extrapolation based approach to address this challenge has been proposed and tested experimentally [26].

Here, we develop a set of new protocols to benchmark quantum simulation of many-body systems. Our protocols are based on symmetries of the target Hamiltonian [27] and the thermalization properties of the time-evolution of the error terms in the experimental Hamiltonian. Our protocols are designs to estimate both the coherent (systematic) errors and non-Markovian errors (Fig. 1). Therefore, we don't assume that the dynamics is unitary. In the next section, we setup the problem and provide examples. In section III we present our results, and in section IV we conclude with a few remarks on possible experimental implementation.

II. PROBLEM SETUP

We consider the following general model of errors. Let H_{target} be the target Hamiltonian, i.e., the Hamiltonian which we intend, acting on N qubits. It is represented by a $2^N \times 2^N$ matrix. The ideal multi-qubit gate generated by time-evolution under this Hamiltonian would be $\Phi_{target} : \rho \mapsto e^{-itH_{target}} \rho e^{itH_{target}}$, where ρ is a mixed state of the N qubits. However, due to errors, the real gate would be:

$$\Phi_{expt} : \rho \mapsto \int d\mu(\epsilon) \rho_\epsilon(t) \quad (1)$$

Here, $\mu(\epsilon)$ is a measure over the space of N -qubit Hamiltonians and $\rho_\epsilon(t)$ is the solution to the equation

$$\dot{\rho}_\epsilon = -i[H_{target} + \epsilon, \rho_\epsilon] + \sum_j L_j \rho_\epsilon L_j^\dagger - \frac{1}{2} \{ \rho_\epsilon, L_j^\dagger L_j \} \quad (2)$$

with $\rho_\epsilon(0) = \rho$. ϵ models the error in the applied Hamiltonian. We assume that this error can vary over samples, i.e., between experimental shots and therefore is modelled by a distribution $\mu(\epsilon)$. The mean value, $\int \epsilon d\mu(\epsilon) = \epsilon_0$ of this distribution, is the systematic error in the Hamiltonian and contributes to the unitary error in the applied gate. The variance, $\int \|\epsilon - \epsilon_0\|^2 d\mu(\epsilon) = \sigma_0^2$ represents the range of fluctuation of the applied Hamiltonian, i.e., the random errors and it contributes to non-Markovian errors in the gate. Here, $\|X\|$ is an operator norm, the choice of which we discuss later. Note that at this point we do not make any assumption regarding the nature of the distribution $\mu(\epsilon)$. It can be arbitrary. One way to conceptualize the distribution μ is to write ϵ in the pauli basis, $P_{\vec{\alpha}}$, with $\vec{\alpha} \in \{0, x, y, z\}^N$ and $P_{\vec{\alpha}} = \sigma_{\alpha_1} \otimes \dots \otimes \sigma_{\alpha_N}$, with $\sigma_0 = \mathbb{1}$.

$$\epsilon = \sum_{\vec{\alpha}} \epsilon_{\vec{\alpha}} P_{\vec{\alpha}} \quad (3)$$

$\epsilon_{\vec{\alpha}}$ are random variables with mean $\langle \epsilon_{\vec{\alpha}} \rangle_\mu = \int \epsilon_{\vec{\alpha}} d\mu(\epsilon)$ and covariance matrix

$$\Sigma_{\vec{\alpha}\vec{\beta}} = \int \epsilon_{\vec{\alpha}} \epsilon_{\vec{\beta}}^\dagger d\mu(\epsilon)$$

And $\sigma_0^2 = \text{Tr}(\Sigma)$, if we use the Schatten 2-norm. Moreover, $\sigma_0^2 = \sigma_{\max}(\Sigma)$ if we use the maximum singular value norm.

L_i are Lindblad jump operators, representing decay processes which contribute to a Markovian error. Through the rest of this paper, we assume that $L_i = 0$, and focus on estimating the unitary and non-Markovian errors (ϵ_0 and σ_0). While this assumption is not experimentally justified, it makes the development of the theory simpler which can then be applied to real experiments after either minimizing or mitigating the Markovian errors. Moreover, the Markovian errors can be measured *independently* and *exclusively* using double stochasticity violation [27].

Here, we focus on the problem of developing a protocol to estimate the first two moments of $\mu(\epsilon)$, i.e., ϵ_0 and σ_0 – that is, to characterize the error generators and measure the fluctuations. We will show that the symmetries of the Hamiltonian H_{target} can be used to develop such protocols. Before proceeding further, we consider two examples of this setup.

Example 1: Rydberg atoms Consider a linear array of Rydberg atoms in a tweezer array. One can simulate a

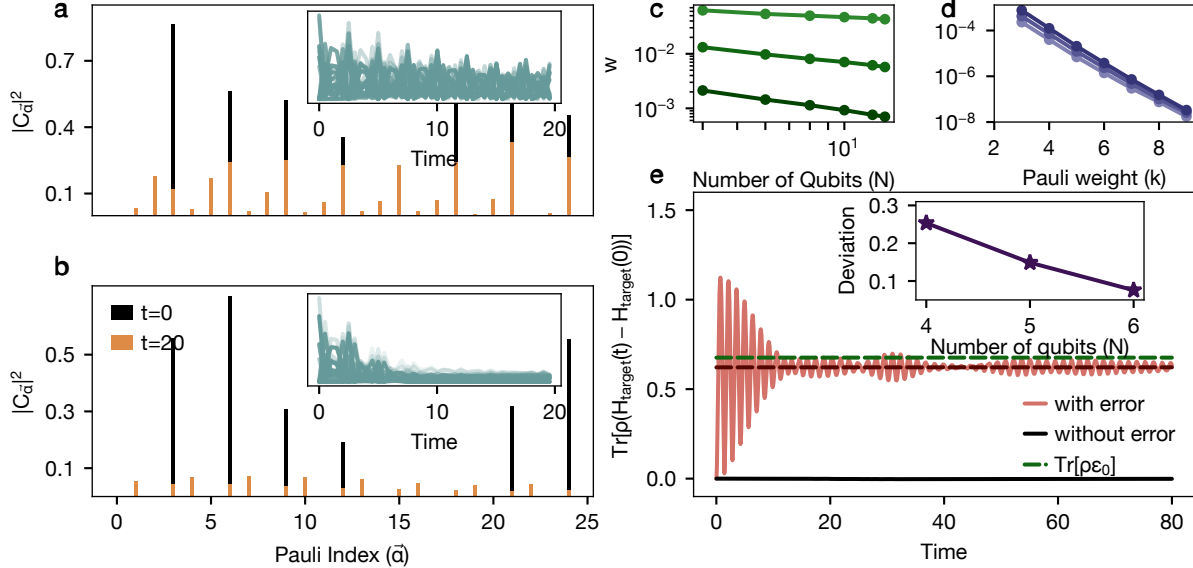


Figure 2. **Operator thermalization and typicality of commuting errors:** **a.** The coefficients $|C_{\vec{\alpha}}(t)|^2$ in $\epsilon(t) = \sum_{\vec{\alpha}} C_{\vec{\alpha}}(t) P_{\vec{\alpha}}$ shown for $t = 0$ (black bars) and long time limit ($t = 20$, orange bars). $C_{\vec{\alpha}}(0)$ we chosen randomly and the time evolution was done with $N = 8$ qubits, under the Hamiltonian in Eq. (4), with $\Omega = 2$ and $\Delta = V = 1$. See ref. [28] for details of the indexing of $\vec{\alpha}$ in the x-axis. Inset shows $|C_{\vec{\alpha}}(t)|^2$ as a function of t , for 20 values of $\vec{\alpha}$. **b.** same as **a**, but with averaging over $\mu(\epsilon)$ computed using Monte-Carlo. Notice that the heights of the orange bars have reduced significantly. See SI for details on the Monte-Carlo. **c.** The weight of the commuting part, w (see text, Eq. (19)) as a function of system size, computed for the Hamiltonian Eq. (4), with $\Omega = 2$, $\Delta = V = 1$ and $N = 8$. The three lines correspond to $k(\vec{\alpha}) = 1, 2, 3$ **d.** w computed for the same Hamiltonian, for random $\vec{\alpha}$'s with different weights. The three lines correspond to $N = 10, 11, 12$. **e.** The time evolution of $\text{Tr}[\rho(H_{\text{target}}(t) - H_{\text{target}}(0))]$ for the case with error (red curve) compared with the case without error (black line). The purple dashed line represents the thermal value and the green dashed line represents $\text{Tr}[\rho\epsilon_0]$. The gap between these two represents the small ϵ_{com} . The computation was done with $N = 7$ and a random ρ in the z -basis. The inset shows the gap between the thermal value and $\text{Tr}[\rho\epsilon_0]$, as a function of system size. See ref. [28] for more details of the data.

transverse field Ising model by using a dressing laser and a rydberg laser. The target Hamiltonian would be

$$H_{\text{target}} = \Omega \sum_j \sigma_{x,j} + \Delta \sum_j \sigma_{z,j} + \sum_i V \sigma_{z,i} \sigma_{z,i+1} \quad (4)$$

Here, $\sigma_{\alpha,j} = \mathbb{1}^{\otimes j-1} \otimes \sigma_{\alpha} \otimes \mathbb{1}^{\otimes (N-j)}$, with $\mathbb{1}$ being the 2×2 identity and $\alpha \in \{x, y, z\}$. This is a weight-1 pauli operator with a σ_{α} in the j -the position and identities on the rest. Ω and Δ are generated by the power and detuning of a coupling laser. V is produced by rydberg blockade, approximated to nearest neighbours, by choosing the blockade radius. In the implementation of this model, the most common forms of errors can be modelled as

$$\begin{aligned} \epsilon = & \sum_j \delta\Omega_j \sigma_{x,j} + \sum_j \delta\Delta_j \sigma_{z,j} \\ & + \sum_{i,j} \delta V_{ij} \sigma_{z,i} \sigma_{z,j} + \sum_{ijk} \delta V_{i,j,k} \sigma_{z,i} \sigma_{z,j} \sigma_{z,k} + \dots \end{aligned} \quad (5)$$

Here, $\delta\Omega_j$ and $\delta\Delta_j$ are random numbers describing the spatial and shot-to-shot variation of the laser power and frequency. δV_{ij} , δV_{ijk} etc. represent the residual Rydberg blockade and any possible multi-qubit interactions,

although the latter can be assumed to be restricted to a 3-qubit terms. They all may be modelled as Gaussian random variables, in which case, $\mu(\epsilon)$ would be a multi-variable Gaussian distribution. If the mean values over several shots of any of these random variables is non-zero, then we will have a systematic error, ϵ_0

$$\begin{aligned} \epsilon_0 = \int \epsilon d\mu(\epsilon) = & \sum_j \langle \delta\Omega_j \rangle_{\mu} \sigma_{x,j} + \sum_j \langle \delta\Delta_j \rangle_{\mu} \sigma_{z,j} \\ & + \sum_{i,j} \langle \delta V_{ij} \rangle_{\mu} \sigma_{z,i} \sigma_{z,j} + \sum_{ijk} \langle \delta V_{i,j,k} \rangle_{\mu} \sigma_{z,i} \sigma_{z,j} \sigma_{z,k} + \dots \end{aligned} \quad (6)$$

Here, $\langle \cdot \rangle_{\mu}$ represents the average of these random variables over the model distribution.

Example 2: Bosons in a lattice: Consider a lattice with N sites loaded with bosonic atoms, typically realized with ultracold atoms in an optical lattice. This system can be used to simulate the Bose-Hubbard model and its

variants. The Hamiltonian is

$$H_{target} = -J \sum_j \hat{a}_j^\dagger \hat{a}_{j+1} + \hat{a}_{j+1}^\dagger \hat{a}_j + \sum_j \Delta_j \hat{a}_j^\dagger \hat{a}_j + \frac{U}{2} \sum_j \hat{a}_j^\dagger \hat{a}_j (\hat{a}_j^\dagger \hat{a}_j - 1) \quad (7)$$

Here, \hat{a}_j^\dagger is the creation operator for site j . J is the hopping rate, controlled by the lattice depth. Δ_j is an on-site potential. When $U \rightarrow \infty$, one can re-write this Hamiltonian in terms of spin-1/2 operators:

$$H_{target} = -\frac{J}{2} \sum_j (\sigma_{x,j} \sigma_{x,j+1} + \sigma_{y,j} \sigma_{y,j+1}) + \sum_j \Delta_j \sigma_{z,j} \quad (8)$$

Here, \hat{a}_j^\dagger is mapped to $\sigma_{+,j}$. The standard errors can be modelled as

$$\epsilon = \sum_{ij} \delta J_{ij} (\sigma_{x,i} \sigma_{x,j} + \sigma_{y,i} \sigma_{y,j}) + \sum_j \delta \Delta_j \sigma_{z,j} \quad (9)$$

Here, δJ_{ij} are random numbers representing errors in the hopping and next nearest neighbour, next-next nearest neighbour hopping, etc. Note that in most cases, hopping processes with a range longer than the next-nearest neighbour are quite insignificant. $\delta \Delta_j$ are random numbers representing on-site potentials due to laser power fluctuations, etc. It is important to note that having double occupancies due to a finite Hubbard interaction U can be a significant source of error. Under the mapping to spin-1/2 system, this will appear as a non-Markovian error due to leakage to other levels. However, one can model these errors effectively by mapping each site to a qudit, instead of a qubit. That is, \hat{a}_j^\dagger can be mapped to S_+ , where the latter is the ladder operator for a d -level system, defined with appropriate coefficients. While they are beyond the scope of this paper, the results here can be generalized to qudits as well. We focus on qubits for the rest of the paper.

We note, in both the above examples, that most physical errors are generated via low-weight Pauli operators. Therefore, in general, one can model the error as an operator within the span of a low-weight Pauli operator. That is,

$$\epsilon = \sum_{k(\vec{\alpha}) \leq m} P_{\vec{\alpha}} \epsilon_{\vec{\alpha}}; \quad \epsilon_0 = \sum_{k(\vec{\alpha}) \leq m} P_{\vec{\alpha}} \langle \epsilon_{\vec{\alpha}} \rangle_{\mu} \quad (10)$$

$k(\vec{\alpha})$ is the number of non-zero entries in $\vec{\alpha}$, i.e., the weight of $P_{\vec{\alpha}}$. Finally, $m \ll N$ is an integer that doesn't scale with N . Practically, one can assume $m \leq 4$.

III. RESULTS

Recall that $\Phi_{target} : \rho \mapsto e^{-itH_{target}} \rho e^{itH_{target}}$ is the target multi-qubit unitary gate, where H_{target} is the N -qubit Hamiltonian and Φ_{expt} is the experimentally realized multi-qubit gate, different from Φ_{target} due to the

errors discussed above, Eq. (2). Note that while Φ_{target} is a unitary map, Φ_{expt} can be a general completely positive trace preserving (CPTP) map. The problem of benchmarking and error characterization is to estimate the difference between Φ_{expt} and Φ_{target} . We show that this can be done using the symmetries of H_{target} , the Hamiltonian generating Φ_{target} .

In particular, if an observable \hat{O} commutes with the target Hamiltonian, i.e., $[H_{target}, \hat{O}] = 0$, it follows that

$$\text{Tr}[\hat{O}(\Phi_{target}(\rho) - \rho)] = 0 \quad (11)$$

for all N -qubit states ρ . For reasons that will be clear soon, we switch to the Heisenberg picture:

$$\text{Tr}[(\hat{O} - \hat{O}(t))\rho] = 0 \quad (12)$$

Here, $\hat{O}(t)$ is the time-evolved operator, defined by $\hat{O}(t) = \tilde{\Phi}_{target}(\hat{O}) = e^{itH_{target}} \hat{O} e^{-itH_{target}}$. Here, $\tilde{\Phi}_{target}$ is the map Φ_{target} in the Heisenberg picture. Similarly, we can define $\tilde{\Phi}_{expt}$, the map Φ_{expt} in the Heisenberg picture. In general, whenever \hat{O} commutes with H_{target} ,

$$\tilde{\Phi}_{expt}(\hat{O}) - \tilde{\Phi}_{target}(\hat{O}) = \tilde{\Phi}_{expt}(\hat{O}) - \hat{O} \quad (13)$$

Note that the RHS of the above equation can be measured experimentally. The problem is to develop a protocol to estimate the first two moments of $\mu(\epsilon)$, i.e., ϵ_0 and σ_0 .

We may choose $\hat{O} = H_{target}, H_{target}^2, \dots$. When H_{target} is a sum of low-weight Pauli operators, its expectation value can be measured efficiently in the lab. In particular, the target Hamiltonian is a sum of Pauli operators up to weight 2; therefore, they can be measured efficiently. Measuring $H_{target}^2, H_{target}^3$ are less efficient. In this paper, we restrict to H_{target} .

After time-evolution, $H_{target}(t) = \tilde{\Phi}_{expt}(H_{target})$ is

$$H_{target}(t) = \int d\mu(\epsilon) e^{it(H_{target} + \epsilon)} H_{target} e^{-it(H_{target} + \epsilon)} \quad (14)$$

Note that $e^{it(H_{target} + \epsilon)} (H_{target} + \epsilon) e^{-it(H_{target} + \epsilon)} = (H_{target} + \epsilon)$. Thus, it follows that

$$H_{target}(t) - H_{target}(0) = \int \epsilon d\mu(\epsilon) - \int \epsilon(t) d\mu(\epsilon) \quad (15)$$

Here, $\epsilon(t) = e^{it(H_{target} + \epsilon)} \epsilon e^{-it(H_{target} + \epsilon)}$. The above expression simplifies to

$$H_{target}(t) - H_{target}(0) = \epsilon_0 - \langle \epsilon(t) \rangle_{\mu} \quad (16)$$

where, $\langle \cdot \rangle_{\mu}$ is the averaging over $\mu(\epsilon)$. For an initial state ρ , one can experimentally measure the expectation $\text{Tr}[\rho(H_{target}(t) - H_{target}(0))]$, which gives us $\text{Tr}[\rho(\epsilon_0 - \langle \epsilon(t) \rangle_{\mu})]$. The latter can be used to characterize ϵ_0 and estimate σ_0 . We begin with characterizing

Protocol 1 (Coherent errors):	Protocol 2 (Coherent errors)
<ul style="list-style-type: none"> • Repeat for $n \in \{1, 2, \dots, m\}$: <ul style="list-style-type: none"> – Repeat for $\vec{\alpha}$ with $k(\vec{\alpha}) = n$: <ul style="list-style-type: none"> * Repeat for $j \in \{1, 2, \dots, r\}$: <ul style="list-style-type: none"> 0 (Repeat for ν samples) 1 Prepare the n qubits corresponding to the non-zero entries in $\vec{\alpha}$ in the corresponding pure single qubit states. 2 Prepare the remaining $N - n$ qubits in an ℓ-bit entangled state (see ref. [31] for details) 3 Apply a set of random single-qubit gates on these $N - n$ qubits. 4 Evolve this initial state under the experimentally implemented target Hamiltonian H_{target}. 5 Apply the single qubit gate on each of the N qubits appropriate to measure H_j. 6 Measure in the z basis. 	<ul style="list-style-type: none"> • Pick p random pure states, represented by points (x_i, y_i, z_i) on the Bloch sphere for $i = 1, 2, \dots, p$ • Repeat for $i \in \{1, 2, \dots, p\}$: <ul style="list-style-type: none"> – Repeat for $j \in \{1, 2, \dots, r\}$: <ul style="list-style-type: none"> 0 (Repeat for ν samples) 1 Prepare all the N qubits in the state represented by (x_i, y_i, z_i) on the Bloch sphere. 2 Evolve this initial state under the experimentally implemented target Hamiltonian H_{target}. 3 Apply the single qubit gate on each of the N qubits appropriate to measure H_j. 4 Measure in the z basis.

Figure 3. Protocols: The left panel shows the first protocol, which assumes single-qubit addressing. This protocol can be used to extract the individual error coefficients $\langle \epsilon_{\vec{\alpha}} \rangle_{\mu}$, for low weight indices $\vec{\alpha}$. The right panel shows a polynomial interpolation protocol, which can be implemented without single-qubit addressing. It can be used to extract the symmetric, i.e., S_N -invariant components $\langle \epsilon_{k_x, k_y, k_z} \rangle_{\mu}$ of the error (see text).

ϵ_0 . This requires understanding the dynamics of $\langle \epsilon(t) \rangle_{\mu}$.

A. Characterizing ϵ_0

Considering Eq. (10), characterizing ϵ_0 involves measuring the average values $\langle \epsilon_{\vec{\alpha}} \rangle_{\mu}$. Corresponding to the pauli operator $P_{\vec{\alpha}}$, let us define a state $\rho_{\vec{\alpha}} = \frac{1}{2^N}(\mathbb{1}^{\otimes N} + P_{\vec{\alpha}})$. It is straightforward to prepare this state for low-weight Pauli operators, given that a large number of the qubits need to be in the maximally mixed state. For example, if $P_{\vec{\alpha}} = \sigma_x \otimes \mathbb{1}^{\otimes N-1}$, in the state $\rho_{\vec{\alpha}}$, the first qubit is in the $|+\rangle$ state and the rest are maximally mixed. We will return to the experimental details of preparing such states with higher Pauli weights later. Note that $\langle \epsilon_{\vec{\alpha}} \rangle_{\mu} = \text{Tr}[\rho_{\vec{\alpha}} \epsilon_0]$. Thus, if we measure $H_{target}(t)$ with the initial state $\rho_{\vec{\alpha}}$, it follows from Eq. (16) that,

$$\text{Tr}[\rho_{\vec{\alpha}}(H_{target}(t) - H_{target}(0))] = \langle \epsilon_{\vec{\alpha}} \rangle_{\mu} - \text{Tr}[\rho_{\vec{\alpha}} \langle \epsilon(t) \rangle_{\mu}] \quad (17)$$

In the following, we will show that under ergodic Hamiltonians, $\text{Tr}[\rho_{\vec{\alpha}} \langle \epsilon(t) \rangle_{\mu}] \approx 0$ in the limit of large t . Thus, $\langle \epsilon_{\vec{\alpha}} \rangle_{\mu} \approx \text{Tr}[\rho_{\vec{\alpha}}(H_{target}(t) - H_{target}(0))]$ and it can be used to characterize the error.

Operator thermalization: The time evolution $\epsilon(t)$ under the Hamiltonian $H_{target} + \epsilon$ can be understood using operator thermalization. We can write ϵ as the sum of a commuting and a non-commuting part with $H_{target} + \epsilon$. That is,

$$\epsilon = \epsilon_{com} + \epsilon_{noncom} \quad (18)$$

where, $[H_{target} + \epsilon, \epsilon_{com}] = 0$. There are three equivalent definitions of ϵ_{com} . (i) ϵ_{com} is the diagonal part of ϵ , written in the eigenbasis of $H_{target} + \epsilon$. That is, assuming that $H_{target} + \epsilon$ is non-degenerate, if $\{|E_n\rangle\}$ are its eigenstates, we define

$$\epsilon_{com} = \sum_n |E_n\rangle \langle E_n| \langle E_n| \epsilon |E_n\rangle$$

More generally, if $H_{target} + \epsilon$ has degeneracies and Π_n are the eigen projectors,

$$\epsilon_{com} = \sum_n \Pi_n \epsilon \Pi_n$$

That is, ϵ_{com} is the diagonal blocks of ϵ in the eigenbasis of $H_{target} + \epsilon$. (ii) ϵ_{com} is the operator that minimizes the distance $\|X - \epsilon\|^2$ over all X that commute with $H_{target} + \epsilon$. And (iii), ϵ_{com} is the projection of ϵ onto the null space of the adjoint map, $\text{ad}_{H_{target} + \epsilon}$. See ref. [28] for details on the equivalence of these three definitions.

Under the time-evolution, $\epsilon(t) = \epsilon_{com} + \epsilon_{noncom}(t)$, i.e., the commuting part does not evolve in time. The mn -th element of $\epsilon_{noncom}(t)$ in the eigenbasis of the Hamiltonian is, $\langle E_n| \epsilon_{noncom}(t) |E_m\rangle = e^{-i(E_n - E_m)t} \langle E_n| \epsilon_{noncom}(0) |E_m\rangle$, the phases of which, in general can be assumed to be nearly random after a long time. Thus, if one writes the time-evolved operator in the Pauli basis, $\epsilon_{noncom}(t) = \sum P_{\vec{\alpha}} C_{\vec{\alpha}}(t)$, the coefficients $C_{\vec{\alpha}}(t) = \frac{1}{2^N} \text{Tr}[P_{\vec{\alpha}} \epsilon_{noncom}(t)]$ would be ex-

ponentially suppressed (Fig. 2a). Moreover, the averaging over $\mu(\epsilon)$ further suppresses $\epsilon_{noncom}(t)$. Fig 2b shows this additional suppression. Therefore, after a sufficiently long time, $\text{Tr}[\rho_{\vec{\alpha}}(H_{target}(t) - H_{target}(0))] \approx \frac{1}{2^N} \text{Tr}[(\epsilon_0 - \epsilon_{com})P_{\vec{\alpha}}]$ and therefore a measurement of the former can be used to characterize $\epsilon_0 - \epsilon_{com}$.

An averaging over time can be used to further suppress the time-dependent part $\epsilon_{noncom}(t)$. It is straightforward to see that

$$\lim_{T \rightarrow \infty} \frac{1}{T} \int_0^T dt \epsilon_{noncom}(t) = 0$$

However, the rate of convergence may vary and has been studied extensively in the theory of operator thermalization. See ref. [28] for a brief discussion.

In general, one cannot eliminate the commuting part ϵ_{com} from the measured projection. That is, any commuting part of the error can't be measured. However, one can show that the commuting part is vanishingly small for experimentally relevant cases. Let us define the magnitude of the commuting part,

$$w = \frac{\|\epsilon_{com}\|^2}{\|\epsilon\|^2} = \frac{\sum_n |\langle E_n | \epsilon | E_n \rangle|^2}{\|\epsilon\|^2}$$

If $\epsilon = \epsilon_{\vec{\alpha}_0} P_{\vec{\alpha}_0}$, a particular Pauli, the weight is

$$w = \frac{\sum_n |\langle E_n | P_{\vec{\alpha}_0} | E_n \rangle|^2}{2^N} \quad (19)$$

Note that while this is the ratio of the magnitude squared of the projection of ϵ onto the null space of $\text{ad}_{H_{target} + \epsilon}$, it can also be understood as the ratio of the projections on to the state $\rho_{\vec{\alpha}}$, i.e., $w = \text{Tr}[\rho_{\vec{\alpha}_0} \epsilon_{com}] / \text{Tr}[\rho_{\vec{\alpha}_0} \epsilon]$. If $|E_n\rangle$ are highly entangled, one can show that w is vanishingly small. To see this, let us consider a random matrix produce state (MPS) with bond dimension χ , $|\psi\rangle$. The eigenstates $|E_n\rangle$ can also be expressed as MPS. It follows from the typicality result for random MPS with a given bond dimension χ from refs [29, 30] that

$$\text{Pr}[|\langle \psi | P_{\vec{\alpha}} | \psi \rangle| \geq \delta] \leq c_1 e^{-c_2 \delta^2 \frac{\chi}{N^2}}$$

Therefore, if the bond dimension of the bulk eigenstates $|E_n\rangle$ grows faster than $O(N^2)$, the typical value of $|\langle \psi | P_{\vec{\alpha}} | \psi \rangle|$ is suppressed to $O\left(\frac{N}{\sqrt{\chi}}\right)$ and so does w .

Fig. 2c shows w as a function of N for $k(\vec{\alpha}) = 1, 2, 3$, for the Hamiltonian from example 1 (Eq. (4)). The data appears to converge polynomially down to zero. Fig. 2d shows w for the same Hamiltonian, for various weights $k(\vec{\alpha})$, which appears to converge exponentially. This observation is also related to the features of operator thermalization. In fact, one can show that if the eigenstates of $H_{target} + \epsilon$ have an entanglement depth of ℓ , i.e., they are ℓ -bit entangled states, then the magnitude of the commuting part w of a Pauli operator with weight k scales as $w \sim \frac{1}{(2^{\ell+1})^k}$ (see [28] for a proof and details). Fig. 2e shows a comparison between $\text{Tr}[\rho_{\vec{\alpha}}(H_{target}(t) - H_{target}(0))]$, its thermal value

$\frac{1}{T} \int_0^T dt \text{Tr}[\rho_{\vec{\alpha}}(H_{target}(t) - H_{target}(0))]$ and the error coefficient $\langle \epsilon_{\vec{\alpha}} \rangle_{\mu}$. We now use these results to construct two explicit protocols to estimate $\langle \epsilon_{\vec{\alpha}} \rangle_{\mu}$.

Protocol 1: The theory developed so far uses the state $\rho_{\vec{\alpha}}$. While this can be produced experimentally, we construct a slightly different state for the protocol in order to minimize the number of sampling rounds. For $\vec{\alpha}$ with $k(\vec{\alpha}) = n$, let $\vec{\alpha}_1, \vec{\alpha}_2, \dots, \vec{\alpha}_n$ be the weight-1 pauli indices such that $P_{\vec{\alpha}} = P_{\vec{\alpha}_1} P_{\vec{\alpha}_2} \dots P_{\vec{\alpha}_n}$. For instance, if $\vec{\alpha} = xy000$, then it's weight is $n = 2$ and $\vec{\alpha}_1 = x0000$ and $\vec{\alpha}_2 = 0y000$. We now define the state $\tilde{\rho}_{\vec{\alpha}} = \frac{1}{2^N} (\mathbb{1}^{\otimes N} + P_{\vec{\alpha}_1})(\mathbb{1}^{\otimes N} + P_{\vec{\alpha}_2}) \dots (\mathbb{1}^{\otimes N} + P_{\vec{\alpha}_N})$. In the above example, $\tilde{\rho}_{\vec{\alpha}} = \frac{1}{2^5} (\mathbb{1} + \sigma_x) \otimes (\mathbb{1} + \sigma_y) \otimes \mathbb{1}^{\otimes 3}$. This state can be prepared with a fidelity of $\sim f^n \left(1 - \frac{1}{\sqrt{\nu} \sqrt{1+2^{\ell}}}\right)$ using single qubit gates of fidelity f and ν sampling rounds and ℓ -bit entangled states, following the protocol presented in ref. [31]. This state also contains $P_{\vec{\alpha}}$ and lower-weight Paulis. It takes fewer samples to produce this state than $\rho_{\vec{\alpha}}$. Let $H_{target} = H_1 + \dots + H_r$, where each H_j is a sum of mutually commuting Paulis. For instance, in example 1, Eq. (4), $H_{target} = H_1 + H_2$ with $H_1 = \Omega \sum_j \sigma_{x,j}$ and $H_2 = \sum_j \Delta \sigma_{z,j} + \sum_j V \sigma_{z,j} \sigma_{z,j+1}$. One needs separate measurement settings to measure each H_j . Protocol 1 is based on measuring each H_j after time evolution of the states $\tilde{\rho}_{\vec{\alpha}}$ and using the result to extract the coefficient $\langle \epsilon_{\vec{\alpha}} \rangle_{\mu}$. We present this protocol in Fig. 3, left panel.

In this protocol, for each n , we need $3^n \binom{N}{n} r$ measurement settings and ν sampling rounds. From these measurement results, one can extract $\langle \epsilon_{\vec{\alpha}} \rangle_{\mu}$ for $k(\vec{\alpha}) \leq m$. The number of measurement settings scales polynomially in N , which could still be nontrivial to implement. Moreover, it also needs single qubit addressing, which is not available in all experiments. Below, we develop a simpler protocol, that doesn't use single-site addressing. That is, we will only use initial states of the form $\rho^{\otimes N}$. However, this protocol can only measure the error components that are invariant under qubit permutations.

A single qubit pure state is represented by a point on the Bloch sphere, represented by three real coordinates (x, y, z) with $x^2 + y^2 + z^2 = 1$. It can be written as $\rho = \frac{1}{2} (\mathbb{1} + x\sigma_x + y\sigma_y + z\sigma_z)$. If all the N qubits are prepared in the same state, the N -qubit state expands as

$$\rho^{\otimes N} = \frac{1}{2^N} \sum_{\vec{\alpha} \in \{0, x, y, z\}^N} x^{k_x(\vec{\alpha})} y^{k_y(\vec{\alpha})} z^{k_z(\vec{\alpha})} P_{\vec{\alpha}} \quad (20)$$

where $k_i(\vec{\alpha})$ is the number of i 's in $\vec{\alpha}$. Note that this is a polynomial in x, y and z and it collects together all the $P_{\vec{\alpha}}$ that are equivalent under the action of the permutation group S_N , forming invariant terms. We define these terms as:

$$Q_{k_x, k_y, k_z} = \sum_{k_i(\vec{\alpha})=k_i} P_{\vec{\alpha}}$$

These Q operators are sums of paulis and they are in-

variant under S_N . Indeed,

$$\rho^{\otimes N} = \frac{1}{2^N} \sum_{k_x, k_y, k_z} x^{k_x} y^{k_y} z^{k_z} Q_{k_x, k_y, k_z}$$

This state, therefore, lives completely in the invariant subspace under the permutation group S_N . Measurements using this state can't be used to determine the variation of the error over the qubits. However, we can always extract the S_N -invariant parts of the error ϵ_0 . It follows that, if we measure the dynamics of the Hamiltonian using this initial state

$$\text{Tr}[\rho^{\otimes N} \epsilon_0] = \sum x^{k_x} y^{k_y} z^{k_z} \langle \epsilon_{k_x, k_y, k_z} \rangle_\mu \text{ where,} \\ \langle \epsilon_{k_x, k_y, k_z} \rangle_\mu = \sum_{k_i(\vec{\alpha})=k_i} \langle \epsilon_{\vec{\alpha}} \rangle_\mu \quad (21)$$

The coefficients $\langle \epsilon_{k_x, k_y, k_z} \rangle_\mu$, which represent the S_N -invariant parts of the error, can be estimated by using a polynomial interpolation of the Hamiltonian dynamics measured for various values of x, y and z . This forms our second protocol (Fig. 3, right panel). This protocol needs pr measurement settings and ν sample rounds. Typically, $r = O(1)$ and p depends on m as $p = O(3^m)$. One can develop variants of this protocol by focussing on the powers of z , for instance, whenever experimentally relevant.

B. Estimating σ_0

We now address the question of how to estimate the canonical non-Markovian errors σ_0 . The non-markovian errors come from the second moment of ϵ , which is implicitly contained in $\langle \epsilon(t) \rangle_\mu$. Indeed, for a specific ϵ and small t ,

$$\epsilon(t) \approx \epsilon - it[H_{\text{target}}, \epsilon] - \frac{t^2}{2}[H_{\text{target}} + \epsilon, [H_{\text{target}}, \epsilon]] + \dots$$

Therefore, the coefficient of t^2 in $\langle \epsilon(t) \rangle_\mu$ contains parts of the second moment of $\mu(\epsilon)$. Indeed, if $\epsilon_0 = 0$,

$$\langle \epsilon(t) \rangle_\mu \approx -\frac{t^2}{2} \langle [\epsilon, [H_{\text{target}}, \epsilon]] \rangle_\mu + O(t^3)$$

This indicates that the information of σ_0 could be extracted from short-time dynamics after correcting for the systematics ϵ_0 . For simplicity, let $\epsilon = \epsilon P$, for a single pauli operator P . The error variable ϵ is a random number with $\langle \epsilon \rangle_\mu = 0$ and $\langle \epsilon^2 \rangle_\mu = \sigma_0^2$. We will show that

$$O(\sigma_0) \leq \max_t \|\langle \epsilon(t) \rangle_\mu\| \leq \sigma_0 \quad (22)$$

Where $\|X\| = \sigma_{\max}(X)$, the maximum singular value. To show the upper bound, note that the time evolution of a particular ϵ is unitary and therefore, $\|\epsilon(t)\| = \|\epsilon\|$. This, along with the triangle inequality, gives

$$\|\langle \epsilon(t) \rangle_\mu\| \leq \int d\mu(\epsilon) \|\epsilon\| \leq \sigma_0$$

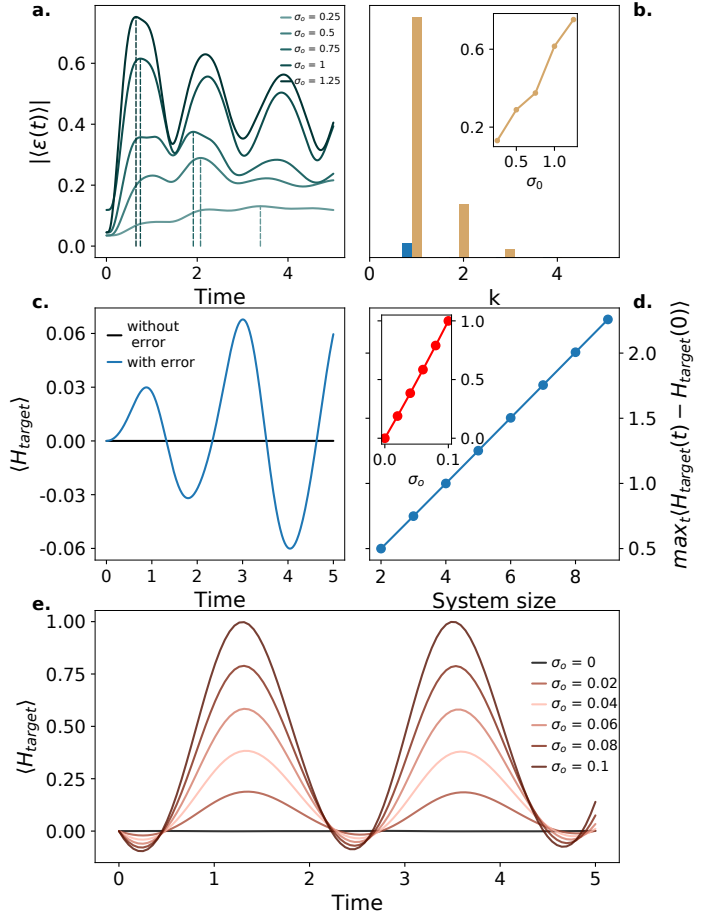


Figure 4. **Numerical experiment:** **a** Time evolution of $\|\epsilon(t)\|$, with five values of σ_0 . **b** Distribution of $\max_t \|\epsilon(t)\|$ across various pauli weights. While the inset presents value of maximum of $\|\epsilon(t)\|$ shown in Fig. 4a versus σ_0 . **c** Time evolution of H_{target} in the short time, with $\epsilon_0 = 0$. **d** The maximum value over time of H_{target} as a function of system size N and σ_0 (inset). The linearity observed here and inequality in Eq. (22), indicate that σ_0 can be directly estimated from short-time measurement of $H_{\text{target}}(t)$ w.r.t various initial states. **e** The time evolution of H_{target} for various σ_0 .

The last inequality follows from the identity $\int |X| \leq \sqrt{\int |X|^2}$. The lower bound for $\max_t \|\epsilon(t)\|$ shows that the above bound is not far away from tightness and that the short time dynamics can be used to estimate σ_0 . We will show that when $t \lesssim \frac{1}{\sigma_0}$,

$$\max_{t \leq \frac{1}{\sigma_0}} \|\langle \epsilon(t) \rangle_\mu\| \gtrsim O(\sigma_0) \quad (23)$$

Let us define $\tilde{\epsilon}(t) = e^{-iH_{\text{target}}t} \epsilon(t) e^{iH_{\text{target}}t} = e^{-iH_{\text{target}}t} e^{i(H_{\text{target}} + \epsilon)t} \epsilon e^{-i(H_{\text{target}} + \epsilon)t} e^{iH_{\text{target}}t}$. For most metrics, $\|\epsilon(t)\| = \|\tilde{\epsilon}(t)\|$. We may use the BCH formula to write

$$e^{-iH_{\text{target}}t} e^{i(H_{\text{target}} + \epsilon)t} = e^{iGt} \quad (24)$$

Protocol 3 (Non-Markovian errors):

- Repeat for $\vec{\alpha}$ with $k(\vec{\alpha}) = n$:
 - Repeat for $t \in \{t_1, t_2, \dots, t_k\}$:
 - * Repeat for $j \in \{1, 2, \dots, r\}$:
 - 0 (Repeat for ν samples)
 - 1 If $\alpha_{i_1}, \dots, \alpha_{i_n}$ are the non-zero characters in $\vec{\alpha}$, prepare the n qubits $\{i_1, \dots, i_n\}$ in a random eigenstate of $\sigma_{\alpha_{i_1}} \otimes \dots \otimes \sigma_{\alpha_{i_n}}$ with eigenvalue +1.
 - 2 Prepare the remaining $N - n$ qubits in an ℓ -bit entangled state (see ref. [31] for details)
 - 3 Apply a set of random single-qubit gates on these $N - n$ qubits.
 - 4 Evolve this initial state under the experimentally implemented target Hamiltonian H_{target} upto time t .
 - 5 Apply the single qubit gate on each of the N qubits appropriate to measure H_j .
 - 6 Measure in the z basis.
 - Estimate $\sigma_{\vec{\alpha}} = \max_i \text{Tr}[\rho_{\vec{\alpha}}(H_{target}(t_i) - H_{target}(0))]$

Figure 5. **Protocol to estimate σ_0 :** This protocol can be used to estimate the magnitude of the fluctuations within a Pauli weight of n , $\sigma_n = \sqrt{\sum_{k(\vec{\alpha})=n} \sigma_{\vec{\alpha}}^2}$ and $\sigma_0^2 = \sum_n \sigma_n^2$.

where, using $\epsilon = \epsilon P$,

$$G = \epsilon X_1 + \epsilon^2 X_2 + \dots$$

with $X_1 = P - i[H_{target}, P] + 1/12[H_{target}, [H_{target}, P]] + \dots$. In order to obtain a quantitatvive estimate of $\|\langle \tilde{\epsilon}(t) \rangle\|$, we consider a Gaussian distribution $\mu(\epsilon)$ with zero mean and a standard deviation of σ_0 . It follows that

$$\langle \tilde{\epsilon}(t) \rangle_\mu = \frac{1}{\sqrt{2\pi\sigma_0}} \int e^{iGt} P e^{-iGt} \epsilon e^{-\epsilon^2/(2\sigma_0^2)} d\epsilon$$

We approximate $e^{iGt} \approx e^{i\epsilon t X_1}$ for $t \lesssim 1/\sigma_0$ and move to the eigenbasis of X_1 , $\{|j\rangle\}$. In this basis,

$$\begin{aligned} \langle \tilde{\epsilon}(t) \rangle_\mu_{ij} &= \frac{1}{\sqrt{2\pi\sigma_0}} \int e^{i\epsilon(\lambda_i - \lambda_j)t} P_{ij} \epsilon e^{-\epsilon^2/(2\sigma_0^2)} d\epsilon \\ &= i e^{-(\lambda_i - \lambda_j)^2 \sigma_0^2 t^2/2} (\lambda_i - \lambda_j) t \sigma_0^2 P_{ij} \end{aligned} \quad (25)$$

where λ_j are the eigenvalues of X_1 . This function is maximized at $t \sim 1/\sigma_0$, and takes a value $\sim O(\sigma_0)$. Thus, with typical values of the matrix elements being $O(\sigma_0)$, so is the maximum singular value. Therefore, it follows that $\max_t \|\epsilon(t)\| \geq O(\sigma_0)$.

We show this result also using a numerical experiment, in Fig. 4. In Fig. 4a, we show the time evolution of $\|\epsilon(t)\|$, under the Schatten 2-norm for $\epsilon = \epsilon \sigma_{z,N/2}$

and gaussian random variable ϵ with five values of σ_0 . Note that the time at which the maximum is reached decreases with increasing σ_0 (dashed lines). In Fig. 4b inset, we show the value of the maximum as a function of σ_0 . The linearity is apparent with $\max_t \|\epsilon(t)\| \approx 0.6\sigma_0$. The main panel shows the distribution of $\max_t \|\epsilon(t)\|$ across various Pauli weights. Note that the evolution under H_{target} is expected to scramble the error $\|\epsilon(t)\|$ across weights, making it nontrivial to measure. However, as we showed earlier, the maximum is reaches at time $\sim 1/\sigma_0$ and if this time is smaller than the thermalization timescale of H_{target} , one can efficiently estimate $\max_t \|\epsilon(t)\|$. In this case, a measurement of $\text{Tr}[\rho(H_{target}(t) - H_{target}(0))]$ can be used to estimate σ_0 , by using $\rho = \rho_{\vec{\alpha}}$ for low-weight $\vec{\alpha}$. See Fig. 5 for a detailed protocol. In Fig. 4c-e, we run a similar numerical experiment with more general error, involving multiple Paulis. We find that the deviation, $H_{target}(t) - H_{target}(0)$ is infact linear in σ_0 even in this case. Thus, a measurement of $\text{Tr}[\rho(H_{target}(t) - H_{target}(0))]$ can be used to estimate σ_0 .

IV. CONCLUSIONS

We have developed a benchmarking technique for quantum simulators that uses measurements of the target Hamiltonian in time. It is effective against coherent errors caused by systematic errors in the Hamiltonian and non-Markovian errors generated by shot-to-shot fluctuations. If ϵ is the error term in the Hamiltonian which fluctuates over experimental shots, our protocols can be used to completely characterize it's average over the fluctuations, $\epsilon_0 = \langle \epsilon \rangle_\mu$ and estimate total variance σ_0^2 . The latter is the trace of the covariance matrix Σ of the errors ϵ . This scheme can be implemented on Rydberg atoms trapped in a tweezer array or on optical lattices loaded with neutral atoms. A major experimental challenge is to characterize and/or mitigate the Markovian errors, which is present in both these systems and which will interfere with the characterization of the errors presented in this paper. The timescales of Markovian errors observed have been long enough to observe even many-body localization dynamics [32]. They can be characterized independently using double-stochasticity violation [27]. Moreover, quantum error mitigation techniques have been developed recently, specifically targeting the Markovian errors generated by coupling to environment [33, 34].

Another important future direction is to extend the theory for time-dependent errors. So far, we have assumed that ϵ is constant in time. However, in real experimental systems, this can potentially vary in time [35]. Developing the protocol for this case would be a possible next step. A more detailed characterization of the covariance matrix Σ would also be useful in order to optimize errors in quantum control. This would be a more challenging future direction.

ACKNOWLEDGEMENTS

We thank Malcolm Boshier, Karatzyna Krzyzanowska and Monika Aidelsburger for fruitful discussions. This work was supported by the Laboratory Directed Research

and Development (LDRD) program of Los Alamos National Lab. A.P. wishes to express his gratitude to his parents for their constant support.

Competing interests The authors declare no competing interests.

[1] I. Bloch, J. Dalibard, and W. Zwerger, Many-body physics with ultracold gases, *Rev. Mod. Phys.* **80**, 885 (2008).

[2] C. Gross and I. Bloch, Quantum simulations with ultracold atoms in optical lattices, *Science* **357**, 995 (2017).

[3] C. Monroe, W. C. Campbell, L.-M. Duan, Z.-X. Gong, A. V. Gorshkov, P. W. Hess, R. Islam, K. Kim, N. M. Linke, G. Pagano, P. Richerme, C. Senko, and N. Y. Yao, Programmable quantum simulations of spin systems with trapped ions, *Rev. Mod. Phys.* **93**, 025001 (2021).

[4] J. Zhang, G. Pagano, P. W. Hess, A. Kyprianidis, P. Becker, H. Kaplan, A. V. Gorshkov, Z.-X. Gong, and C. Monroe, Observation of a many-body dynamical phase transition with a 53-qubit quantum simulator, *Nature* **551**, 601–604 (2017).

[5] R. Blatt and C. F. Roos, Quantum simulations with trapped ions, *Nature Physics* **8**, 277–284 (2012).

[6] S. Ebadi, T. T. Wang, H. Levine, A. Keesling, G. Semeghini, A. Omran, D. Bluvstein, R. Samajdar, H. Pichler, W. W. Ho, S. Choi, S. Sachdev, M. Greiner, V. Vuletić, and M. D. Lukin, Quantum phases of matter on a 256-atom programmable quantum simulator, *Nature* **595**, 227 (2021).

[7] H. Bernien, S. Schwartz, A. Keesling, H. Levine, A. Omran, H. Pichler, S. Choi, A. S. Zibrov, M. Endres, M. Greiner, V. Vuletić, and M. D. Lukin, Probing many-body dynamics on a 51-atom quantum simulator, *Nature* **551**, 579 (2017).

[8] A. Parra-Rodríguez, P. Lougovski, L. Lamata, E. Solano, and M. Sanz, Digital-analog quantum computation, *Phys. Rev. A* **101**, 022305 (2020).

[9] M. G. de Andoin, Álvaro Saiz, P. Pérez-Fernández, L. Lamata, I. Oregi, and M. Sanz, Digital-analog quantum computation with arbitrary two-body hamiltonians (2023), [arXiv:2307.00966 \[quant-ph\]](https://arxiv.org/abs/2307.00966).

[10] B. Hebbe Madhusudhana, S. Scherg, T. Kohlert, I. Bloch, and M. Aidelsburger, Benchmarking a novel efficient numerical method for localized 1d fermi-hubbard systems on a quantum simulator, *PRX Quantum* **2**, 040325 (2021).

[11] A. J. Daley, I. Bloch, C. Kokail, S. Flannigan, N. Pearson, M. Troyer, and P. Zoller, Practical quantum advantage in quantum simulation, *Nature* **607**, 667 (2022).

[12] E. Nielsen, J. K. Gamble, K. Rudinger, T. Scholten, K. Young, and R. Blume-Kohout, Gate set tomography, *Quantum* **5**, 557 (2021).

[13] E. Magesan, J. M. Gambetta, and J. Emerson, Scalable and robust randomized benchmarking of quantum processes, *Phys. Rev. Lett.* **106**, 180504 (2011).

[14] E. Knill, D. Leibfried, R. Reichle, J. Britton, R. B. Blakestad, J. D. Jost, C. Langer, R. Ozeri, S. Seidelin, and D. J. Wineland, Randomized benchmarking of quantum gates, *Phys. Rev. A* **77**, 012307 (2008).

[15] T. J. Proctor, A. Carignan-Dugas, K. Rudinger, E. Nielsen, R. Blume-Kohout, and K. Young, Direct randomized benchmarking for multiqubit devices, *Phys. Rev. Lett.* **123**, 030503 (2019).

[16] T. Proctor, K. Rudinger, K. Young, E. Nielsen, and R. Blume-Kohout, Measuring the capabilities of quantum computers, *Nature Physics* **18**, 75 (2021).

[17] A. Elben, B. Vermersch, R. van Bijnen, C. Kokail, T. Brydges, C. Maier, M. K. Joshi, R. Blatt, C. F. Roos, and P. Zoller, Cross-platform verification of intermediate scale quantum devices, *Phys. Rev. Lett.* **124**, 010504 (2020).

[18] J. Carrasco, A. Elben, C. Kokail, B. Kraus, and P. Zoller, Theoretical and experimental perspectives of quantum verification, *PRX Quantum* **2**, 010102 (2021).

[19] E. Bairey, I. Arad, and N. H. Lindner, Learning a local hamiltonian from local measurements, *Phys. Rev. Lett.* **122**, 020504 (2019).

[20] Z. Li, L. Zou, and T. H. Hsieh, Hamiltonian tomography via quantum quench, *Phys. Rev. Lett.* **124**, 160502 (2020).

[21] J. Wang, S. Paesani, R. Santagati, S. Knauer, A. A. Gentile, N. Wiebe, M. Petruzzella, J. L. O'Brien, J. G. Rarity, A. Laing, and M. G. Thompson, Experimental quantum hamiltonian learning, *Nature Physics* **13**, 551 (2017).

[22] W. Yu, J. Sun, Z. Han, and X. Yuan, Robust and efficient hamiltonian learning, *Quantum* **7**, 1045 (2023).

[23] J. S. Cotler, D. K. Mark, H.-Y. Huang, F. Hernández, J. Choi, A. L. Shaw, M. Endres, and S. Choi, Emergent quantum state designs from individual many-body wave functions, *PRX Quantum* **4**, 10.1103/prxquantum.4.010311 (2023).

[24] J. Choi, A. L. Shaw, I. S. Madjarov, X. Xie, R. Finkelstein, J. P. Covey, J. S. Cotler, D. K. Mark, H.-Y. Huang, A. Kale, H. Pichler, F. G. S. L. Brandão, S. Choi, and M. Endres, Preparing random states and benchmarking with many-body quantum chaos, *Nature* **613**, 468 (2023).

[25] D. K. Mark, J. Choi, A. L. Shaw, M. Endres, and S. Choi, Benchmarking quantum simulators using ergodic quantum dynamics (2023), [arXiv:2205.12211 \[quant-ph\]](https://arxiv.org/abs/2205.12211).

[26] A. L. Shaw, Z. Chen, J. Choi, D. K. Mark, P. Scholl, R. Finkelstein, A. Elben, S. Choi, and M. Endres, Benchmarking highly entangled states on a 60-atom analog quantum simulator (2023), [arXiv:2308.07914 \[quant-ph\]](https://arxiv.org/abs/2308.07914).

[27] B. H. Madhusudhana, Benchmarking multi-qubit gates – ii: Computational aspects (2023), [arXiv:2301.07109 \[quant-ph\]](https://arxiv.org/abs/2301.07109).

[28] See Supplemental Material which includes Refs. [36–44], not cited in the main text, for details on: the definitions of the commuting part, details on operator thermalization, typicality of the commuting part, short time dynamics, other symmetries of the Hamiltonian and details of how the data shown in the main text were obtained.

- [29] S. Garnerone, T. R. de Oliveira, and P. Zanardi, Typicality in random matrix product states, *Phys. Rev. A* **81**, 032336 (2010).
- [30] S. Garnerone, T. R. de Oliveira, S. Haas, and P. Zanardi, Statistical properties of random matrix product states, *Phys. Rev. A* **82**, 052312 (2010).
- [31] B. H. Madhusudhana, Benchmarking multi-qubit gates – i: Metrological aspects (2023), [arXiv:2210.04330 \[quant-ph\]](https://arxiv.org/abs/2210.04330).
- [32] S. Scherg, T. Kohlert, P. Sala, F. Pollmann, B. H. Madhusudhana, I. Bloch, and M. Aidelsburger, Observing non-ergodicity due to kinetic constraints in tilted fermi-hubbard chains, *Nature Communications* **12**, 4490 (2021).
- [33] B. I. C. Donvil, R. Lechler, J. Ankerhold, and P. Muratore-Ginanneschi, Quantum trajectory approach to error mitigation (2023), [arXiv:2305.19874 \[quant-ph\]](https://arxiv.org/abs/2305.19874).
- [34] J. Sun, X. Yuan, T. Tsunoda, V. Vedral, S. C. Benjamin, and S. Endo, Mitigating realistic noise in practical noisy intermediate-scale quantum devices, *Phys. Rev. Appl.* **15**, 034026 (2021).
- [35] T. Kohlert, S. Scherg, P. Sala, F. Pollmann, B. Hebbe Madhusudhana, I. Bloch, and M. Aidelsburger, Exploring the regime of fragmentation in strongly tilted fermi-hubbard chains, *Phys. Rev. Lett.* **130**, 010201 (2023).
- [36] J. M. Deutsch, Quantum statistical mechanics in a closed system, *Physical Review A* **43**, 2046 (1991).
- [37] M. Srednicki, Chaos and quantum thermalization, *Physical Review E* **50**, 888 (1994).
- [38] M. Rigol, V. Dunjko, and M. Olshanii, Thermalization and its mechanism for generic isolated quantum systems, *Nature* **452**, 854 (2008).
- [39] L. D'Alessio, Y. Kafri, A. Polkovnikov, and M. Rigol, From quantum chaos and eigenstate thermalization to statistical mechanics and thermodynamics, *Advances in Physics* **65**, 239 (2016).
- [40] J. M. Deutsch, Eigenstate thermalization hypothesis, *Reports on Progress in Physics* **81**, 082001 (2018).
- [41] P. Sabella-Garnier and et al., Thermalization/relaxation in integrable and free field theories: An operator thermalization hypothesis, [arXiv.org](https://arxiv.org/).
- [42] A. Bukva, P. Sabella-Garnier, and K. Schalm, Operator thermalisation in $d > 2$: Huygens or resurgence, *Journal of High Energy Physics* **2020**, 103 (2020).
- [43] X. Cao, T. Scaffidi, and E. Altman, A universal operator growth hypothesis, *Physical Review X* **9**, 041017 (2019).
- [44] B. Craps and F. Van den Clerck, Energy-level splitting for weakly interacting bosons in a harmonic trap, *Physical Review A* **100**, 023605 (2019).

Supplementary Information

CONTENTS

Acknowledgements	9
References	9
S1. Definitions of the commuting part	S1
1. Algebra of the commuting part	S1
S2. Operator thermalization	S2
S3. Typicality of the commuting part	S3
S4. Short time dynamics	S3
S5. Measuring other symmetries of the Hamiltonian	S3
1. Higher powers of H_{target}	S4
S6. Main text figures	S4
1. Main text figure 2	S4
2. Main text figure 4	S5

Appendix S1: Definitions of the commuting part

In this section, we will show the equivalence of the three definitions of the commuting part A_{com} of an operator A with respect to a given operator M .

Definition 1: If $\{\Pi_n\}$ are the eigen projectors of M ,

$$A_{\text{com}} = \sum_n \Pi_n A \Pi_n$$

Definition 2: A_{com} is the operator that minimizes the function $f(X) = \|X - A\|^2$ over all operators X that commute with M .

Definition 3: A_{com} is the projection of A onto the null space of the superoperator ad_M .

We begin by showing the equivalence of definitions 1 and 2. We write A as

$$A = \sum_n \Pi_n A \Pi_n + Q$$

where $Q = A - \sum_n \Pi_n A \Pi_n$. Hereafter, we refer to the operator $\sum_n \Pi_n A \Pi_n$ as P . This is indeed the A_{com} according to definition 1. The goal is to show that P is the commuting part of A with M , according to definition 2 as well. We begin by showing that P and Q are orthogonal parts of A . Indeed,

$$\begin{aligned} \text{Tr}[PQ] &= \text{Tr}\left[\left(\sum_n \Pi_n A \Pi_n\right)\left(A - \sum_m \Pi_m A \Pi_m\right)\right] \\ &= \sum_n \text{tr}[\Pi_n A \Pi_n A] - \sum_{m,n} \text{Tr}[\Pi_n A \Pi_n \Pi_m A \Pi_m] \end{aligned} \tag{S1}$$

Using the orthogonality of the projectors, $\Pi_n \Pi_m = 0$ unless $n = m$. Therefore,

$$\text{Tr}[PQ] = \sum_n \text{tr}[\Pi_n A \Pi_n A] - \sum_n \text{Tr}[\Pi_n A \Pi_n^2 A \Pi_n]$$

We now use the fact that $\Pi_n^2 = \Pi_n$ and that $\text{Tr}[\Pi_n A \Pi_n^2 A \Pi_n] = \text{Tr}[\Pi_n \Pi_n A \Pi_n^2 A]$, to show that the above is zero. If X is an operator that commutes with M , it follows that

$$X = \sum_n \Pi_n X \Pi_n$$

Therefore,

$$\begin{aligned} \|X - A\|^2 &= \text{Tr}[(X - A)(X - A)] = \text{Tr}[A^2] + \text{Tr}[X^2] - 2\text{Tr}[XA] \\ &= \text{Tr}[A^2] + \sum_n [X^2] - 2 \sum_n \text{Tr}[\Pi_n X \Pi_n A] \end{aligned} \tag{S2}$$

We can now use the cyclic permutation rule of commutators:

$$\begin{aligned} \|X - A\|^2 &= \text{Tr}[A^2] + \text{Tr}[X^2] - 2 \sum_n \text{Tr}[X \Pi_n A \Pi_n] \\ &= \text{Tr}[A^2] + \text{Tr}[X^2] - 2\text{Tr}[XP] \\ &= \text{Tr}[A^2] - \text{Tr}[P^2] + \|P - X\|^2 \end{aligned} \tag{S3}$$

Note that P commutes with M and therefore, $X = P$ is a legitimate choice. This function is quadratic and is minimized when $X = P$. Thus, definition 2 gives the same result as definition 1.

Finally, we will show that definition 3 is equivalent to definition 2. The adjoint map ad_M is defined as

$$\text{ad}_M(X) = [M, X]$$

Therefore, the null space of the superoperator ad_M is the space of all operators that commute with M . Therefore, the projection of A onto this space is indeed the operator from this space that minimizes $\|A - X\|^2$, which is the commuting part according to definition 2.

1. Algebra of the commuting part

In this section, we discuss some of the basic algebraic properties of the commuting part of an operator w.r.t. a given operator.

Lemma 1: If M is a given operator, for operators A , B , it follows that

$$\text{i. } (A + B)_{\text{com}} = A_{\text{com}} + B_{\text{com}}$$

$$\text{ii. } (AB)_{\text{com}} = A_{\text{com}}B_{\text{com}} + (A_{\text{noncom}}B_{\text{noncom}})_{\text{com}}$$

Where the commuting part is defined w.r.t. M .

Proof: We use the first definition of the commuting part. If Π_n are the eigen projectors of M ,

$$\begin{aligned} (A + B)_{\text{com}} &= \sum_n \Pi_n (A + B) \Pi_n \\ &= \sum_n \Pi_n A \Pi_n + \Pi_n B \Pi_n = A_{\text{com}} + B_{\text{com}} \end{aligned} \quad (\text{S4})$$

Moreover, note that

$$\begin{aligned} A_{\text{noncom}} &= A - \sum_n \Pi_n A \Pi_n = \sum_n \Pi_n A - \sum_n \Pi_n A \Pi_n \\ &= \sum_n \Pi_n A (1 - \Pi_n) \end{aligned} \quad (\text{S5})$$

$$\begin{aligned} A_{\text{com}}B_{\text{com}} &= \sum_{n,m} \Pi_n A \Pi_n \Pi_m B \Pi_m \\ &= \sum_n \Pi_n A \Pi_n B \Pi_n \\ &= (AB)_{\text{com}} - \sum_n \Pi_n A (1 - \Pi_n) B \Pi_n \\ &= (AB)_{\text{com}} - \sum_n \Pi_n A (1 - \Pi_n) (1 - \Pi_n) B \Pi_n \\ &= (AB)_{\text{com}} - \sum_n \Pi_n (A_{\text{noncom}} B_{\text{noncom}}) \Pi_n \\ &= (AB)_{\text{com}} - (A_{\text{noncom}} B_{\text{noncom}})_{\text{com}} \end{aligned} \quad (\text{S6})$$

The last equation follows from the fact that $\Pi_n \Pi_m = 0$ if $n \neq m$.

Appendix S2: Operator thermalization

In this section, we present a brief overview of the theory of operator thermalization. The investigation into how isolated, unitary quantum systems can appear to attain thermal equilibrium has long been a central concern within the field of statistical mechanics, with one of its cornerstones being the eigenstate thermalization hypothesis(ETH) [36–40]. However, considering the Heisenberg picture of evolution, recently, interest has shifted from states to operators, thus introducing the Operator Thermalization Hypothesis (OTH), which was first prominently mentioned in the ref. [41]. A meaningful comparison between ETH and OTH is presented in [42], where the authors use the transverse field Ising model to demonstrate examples exhibiting similarities and differences between ETH and OTH. The authors draw a parallel between ETH and OTH, elucidating that ETH

leads to thermalization due to a chaotic spectrum allowing extensive Hilbert space exploration even with a simple operator, while OTH, as its counterpart, features an organized spectrum, requiring a complex operator for similar exploration. For further investigation, the reader is encouraged to check [41, 43, 44].

Let \hat{O} be any operator acting on a quantum system, which evolves according to Hamiltonian H . Under the Heisenberg picture, the operator evolves in time as $\hat{O}(t) = e^{iHt} \hat{O} e^{-iHt}$. To understand this time evolution, let us write the operator as a sum of the commuting and the non-commuting parts w.r.t. H , as defined above: $\hat{O} = \hat{O}_{\text{com}} + \hat{O}_{\text{noncom}}$. The commuting part is time-invariant. Therefore,

$$\hat{O}(t) = \hat{O}_{\text{com}} + \hat{O}_{\text{noncom}}(t) = \hat{O}_{\text{com}} + e^{iHt} \hat{O}_{\text{noncom}} e^{-iHt}$$

We now show that

$$\lim_{T \rightarrow \infty} \frac{1}{T} \int_0^T \hat{O}(t) = \hat{O}_{\text{com}}$$

That is, the non-commuting part of the operator vanishes in the thermal limit. To see this, note that the ij -th element, in the eigenbasis of H_{target} , of $\hat{O}_{\text{noncom}}(t)$ is

$$\langle i | \hat{O}_{\text{noncom}}(t) | j \rangle = e^{i(\mathcal{E}_i - \mathcal{E}_j)t} \langle i | \hat{O}_{\text{noncom}} | j \rangle, \quad \mathcal{E}_i \neq \mathcal{E}_j$$

Note that when $\mathcal{E}_i = \mathcal{E}_j$, $\langle i | \hat{O}_{\text{noncom}} | j \rangle = 0$. It now follows that the time average of the non-commuting part vanishes in the limit of large T .

The question of the rate and nature of this convergence is a more complex one, for it depends on the distribution of the gaps, $\mathcal{E}_i - \mathcal{E}_j$. These gaps are infact the eigenvalues of ad_H . The existence of a large number of very small gaps implies very long-time non-trivial dynamics and slow convergence to the thermal value.

Appendix S3: Typicality of the commuting part

In this section, we discuss the connection between thermalization and the typical values of the weight of the commuting part. Let $P_{\vec{\alpha}}$ be a pauli operator and H be a many-body Hamiltonian. If $|\mathcal{E}_n\rangle$ are the eigenstates of H , the magnitude w of the commuting part of $P_{\vec{\alpha}}$ w.r.t H is given by

$$w_{\vec{\alpha}} = \frac{1}{2^N} \sum_n (\text{Tr}[P_{\vec{\alpha}} |\mathcal{E}_n\rangle \langle \mathcal{E}_n|])^2$$

This can be understood as the second moment of the coefficients of $P_{\vec{\alpha}}$ in the density matrices $|\mathcal{E}_n\rangle \langle \mathcal{E}_n|$. That is, if we write

$$|\mathcal{E}_n\rangle \langle \mathcal{E}_n| = \sum_{\vec{\beta}} P_{\vec{\beta}} C_{\vec{\beta},n}$$

the magnitude of the commuting part is

$$w_{\vec{\alpha}} = 4^N \langle C_{\vec{\alpha},n}^2 \rangle_{\{n\}}$$

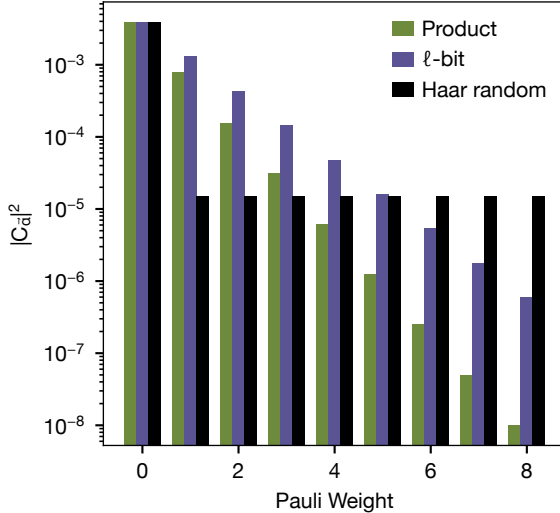


Figure S1. **Entanglement and Pauli coefficients:** The average of $|C_{\vec{\alpha}}|^2$ over various ensembles. For Haar random states, it takes a uniform value, $\frac{1}{4^N(2^N+1)}$. For ℓ -bit states, it falls off exponentially $\frac{1}{4^N(2^\ell+1)^k}$ (see text).

Here, the average is over the eigenstates of H . We can now show some typicality results, if we assume that the eigenstates of H form a 2-design corresponding to some underlying distribution of states. For instance, we can consider random states with a fixed entanglement. We first begin with the simple case of Haar random states. The second moment of $C_{\vec{\alpha}}$ over Haar random states is straightforward to compute. Under Haar randomness, $\langle C_{\vec{\alpha}}^2 \rangle$ must be independent of $\vec{\alpha}$. Moreover, $C_{\vec{0}} = 1/2^N$ and

$$\sum_{\vec{\alpha}} C_{\vec{\alpha}}^2 = \frac{1}{2^N}$$

Combining the two, we obtain:

$$\langle C_{\vec{\alpha}}^2 \rangle = \frac{1}{2^N(4^N-1)} \left(1 - \frac{1}{2^N}\right) = \frac{1}{4^N(2^N+1)}$$

However, the eigenstates of most Hamiltonians are not 2-designs of Haar random states. They are more likely to have a fixed entanglement, but not highly entangled unlike Haar random states. Let us consider the case of products of ℓ -bit Haar random states, i.e., a tensor product of $m = N/\ell$ states, each an ℓ -bit Haar random state. Let $\vec{\alpha} = (\vec{\alpha}_1, \dots, \vec{\alpha}_m)$ where each $\vec{\alpha}_i \in \{0, x, y, z\}^\ell$. It follows that

$$\langle C_{\vec{\alpha}}^2 \rangle = \langle C_{\vec{\alpha}_1}^2 \rangle \langle C_{\vec{\alpha}_2}^2 \rangle \cdots \langle C_{\vec{\alpha}_m}^2 \rangle$$

Moreover, if the pauli weight $k(\vec{\alpha}) = k$, at-most $m-k$ of $\langle C_{\vec{\alpha}_i}^2 \rangle$ s are $1/4^\ell$. Therefore,

$$\langle C_{\vec{\alpha}}^2 \rangle \leq \frac{1}{4^{\ell(m-k)}} \frac{1}{4^{\ell k} (2^\ell+1)^k} = \frac{1}{4^N (2^\ell+1)^k}$$

Thus, in general, the weight $w \lesssim \frac{1}{(2^\ell+1)^k}$ falls down exponentially in k (Fig. S1), as seen in Figure 2d of the main text.

Appendix S4: Short time dynamics

In this section, we show a few basic results on the short time dynamics of $\|\epsilon_0 - \langle \epsilon(t) \rangle_\mu\|$. We first show an upper bound on its magnitude

$$\|\epsilon_0 - \langle \epsilon(t) \rangle_\mu\| \leq \|\epsilon_0\| + \left\| \int d\mu(\epsilon) \epsilon(t) \right\|$$

The time evolution of a particular ϵ is unitary and therefore, $\|\epsilon(t)\| = \|\epsilon\|$. This, along with the triangle inequality gives

$$\|\epsilon_0 - \langle \epsilon(t) \rangle_\mu\| \leq \|\epsilon_0\| + \int d\mu(\epsilon) \|\epsilon\| \leq \|\epsilon_0\| + \sqrt{\|\epsilon_0\|^2 + \sigma_0^2}$$

The last inequality follows from the identity $\int |X| \leq \sqrt{\int |X|^2}$.

Appendix S5: Measuring other symmetries of the Hamiltonian

In this section, we discuss the case of using other operators that commute with H_{target} . If \hat{O} any operator that commutes with H_{target} , we will show an expression similar to Eq. (16) of main text, corresponding to the time evolution of the operator under $H_{target} + \epsilon$. One can define δ as the non-commuting part of \hat{O} w.r.t $H_{target} + \epsilon$. Note that $\delta = 0$ when $\epsilon = 0$. It follows that

$$\hat{O}(t) - \hat{O}(0) = \delta - \delta(t) \quad (S1)$$

If H_{target} doesn't have any degeneracies (or if \hat{O} and H_{target} have the same structure of degenerate blocks), we can show that $\|\delta\| = O(\|\epsilon\|)$. Indeed, if $\{|\psi_n\rangle\}$ are the common eigenstates of H_{target} and \hat{O} and $\{|\tilde{\psi}_n\rangle\}$ are the eigenstates of $H_{target} + \epsilon$, in the absence of degeneracies in the eigenvalues of H_{target} , it follows that

$$|\tilde{\psi}_n\rangle = |\psi_n\rangle + O(\|\epsilon\|)$$

Therefore, the non-commuting part δ or \hat{O} is ($m \neq n$)

$$\delta_{mn} = \langle \tilde{\psi}_m | \hat{O} | \tilde{\psi}_n \rangle = O(\|\epsilon\|) \quad (S2)$$

Therefore, one can use Eq. (S1) to estimate $\|\epsilon\|$ by measuring $\hat{O}(t) - \hat{O}(0)$ in these cases. The magnitude of δ is much more complicated if H_{target} has degeneracies where \hat{O} doesn't. For instance, the error can be magnified in this case.

1. Higher powers of H_{target}

In this section, we consider the idea of measuring higher powers of H_{target} in order to estimate ϵ . We show that while measuring H_{target}^k more data-expensive, it is more sensitive to the error. In fact, the sensitivity increases exponentially in k . In section S2, we showed that the thermal value of any operator is its commuting part. Indeed,

$$\lim_{T \rightarrow \infty} \frac{1}{T} \int_0^T H_{target}^k(t) - H_{target}^k(0) = (H_{target}^k)_{com} - H_{target}^k$$

We now use $(H_{target} + \epsilon)_{com}^k = (H_{target} + \epsilon)^k$. Thus, using what we showed in section S1,

$$(H_{target} + \epsilon)_com^k = (H_{target})_{com}^k + (\epsilon H_{target}^{k-1})_{com} + \dots$$

Therefore,

$$(H_{target}^k)_{com} - H_{target}^k = (\epsilon H_{target}^{k-1})_{com} + \dots$$

For higher values of k , the magnitude of the leading order is about $O(k||H_{target}||^{k-1}||\epsilon_{noncom}||)$. Therefore, the sensitivity increases exponentially in k . However, measuring the terms in H_{target}^k would require much larger dataset – also exponential in k . Moreover, unlike for the case of $k = 1$, it is nontrivial to estimate the various components of ϵ using measurements of H_{target}^k .

Appendix S6: Main text figures

In this section, we provide more details on how the data in the figures of main text were produced.

1. Main text figure 2

In figure 2a, we used a Hamiltonian

$$H_{target} = \Omega \sum_j \sigma_{x,j} + \Delta \sum_j \sigma_{z,j} + V \sum_j \sigma_{j,z} \sigma_{j+1,z},$$

$$\Omega = 2, \Delta = 1 \text{ and } V = 1 \quad (\text{S1})$$

We use $dN = 8$ qubits and a fixed error given by

$$\epsilon = \sum_j \epsilon_j \sigma_{z,j}$$

where ϵ_j are a randomly chosen, fixed set of numbers. We used an initial state $\rho = \frac{1}{2^N} (1 + \sigma_z)^{\otimes N}$. i.e., all qubits in the state $|1\rangle$. We evolve ϵ under $H_{target} + \epsilon$ in time and obtain the coefficients $C_{\vec{\alpha}}(t) = \frac{1}{2^N} \text{Tr}[\epsilon(t) P_{\vec{\alpha}}]$. The main panel shows $|C_{\vec{\alpha}}(0)|^2$ as the black bars, for the 24 values of $\vec{\alpha}$ such that $k(\vec{\alpha}) = 1$. These coefficients are given by $C_{\vec{\alpha}}(0) = \epsilon_j$ for $\vec{\alpha} = (0, 0, \dots, 0, z, 0, \dots, 0)$, where the z is in the j -th position. The $\vec{\alpha}$ s are

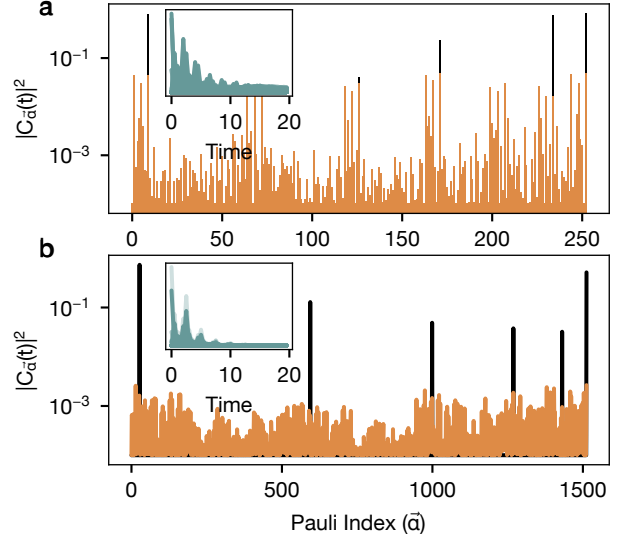


Figure S2. **Operator thermalization:** **a** shows $|C_{\vec{\alpha}}(t)|^2$ for $t = 0$ (black) and $t = 20$ (orange) for $k(\vec{\alpha}) = 2$ and $n = 8$. **b** shows the same for $k(\vec{\alpha}) = 3$.

ordered as $(x, 0, 0, \dots, 0), (y, 0, 0, \dots, 0), (z, 0, 0, \dots, 0), (0, x, 0, \dots, 0), \dots, (0, 0, \dots, 0, z)$ on the x-axis. The orange bars shows $|C_{\vec{\alpha}}(t)|^2$. One can also look at $C_{\vec{\alpha}}(t)$ for higher weight $\vec{\alpha}$, but the picture remains the same. The inset shows the time evolution of these coefficients, for all 24 values of $\vec{\alpha}$.

Similar numerical analysis for $k(\vec{\alpha}) = 2, 3$ is shown in Fig. S2a and Fig. S2b respectively. The error ϵ in these datasets were of the form $\sum_j \epsilon_j \sigma_{z,j} \sigma_{z,j+1}$ and $\sum_j \epsilon_j \sigma_{z,j} \sigma_{z,j+1} \sigma_{z,j+2}$ respectively.

In Figure 2b, we average the results of figure 2a over 40 samples, chosen at random, from a gaussian ensemble of ϵ_j . The mean value of this ensemble is a set of randomly chosen fixed set of numbers. The standard deviation was set at 0.1.

In Figure 2c, we choose three pauli operators $P_1 = \mathbb{1}^{\otimes N/2} \otimes \sigma_z \otimes \mathbb{1}^{\otimes N/2-1}$, $P_2 = \mathbb{1}^{\otimes N/2-1} \otimes \sigma_z \otimes \sigma_z \otimes \mathbb{1}^{\otimes N/2-1}$ and $P_3 = \mathbb{1}^{\otimes N/2-1} \otimes \sigma_z \otimes \sigma_z \otimes \sigma_z \otimes \mathbb{1}^{\otimes N/2-2}$ and compute the weight of their non-commuting parts, w w.r.t the Hamiltonian in Eq. (S1). We use $L = 4, 6, 8, 10, 12, 13$.

In Figure 2d, we compute the weights of paulis $P_k = \mathbb{1}^{\otimes (N-k)/2} \otimes \sigma_{\alpha_1} \otimes \dots \otimes \sigma_{\alpha_k} \mathbb{1}^{\otimes (N-k)/2}$, where $\alpha_1, \dots, \alpha_k$ are randomly chosen from $\{x, y, z\}$. We choose $k = 3, 4, 5, 6, 7, 8, 9$ and $N = 10, 11, 12$.

In Figure 2e main panel, we compute $\text{Tr}[\rho(H_{target}(t) - H_{target}(0))]$ for $N = 7$. The error was modelled as

$$\epsilon = \epsilon_x \sum_i \sigma_{x,i} + \epsilon_y \sum_i \sigma_{y,i} + \epsilon_z \sum_i \sigma_{z,i} \quad (\text{S2})$$

Where ϵ_x, ϵ_y and ϵ_z are random numbers chosen with a randomly chose, and fixed mean value and a standard deviation of 0.1. We use the Hamiltonian in Eq. (S1) and average the resulting time trace over 100 samples.

The state ρ is $\frac{1}{2^N}(\mathbb{1} - \sigma_z)^{\otimes N}$.

2. Main text figure 4

In the following subsection, the numerical details for the Fig. 4 in the main text are discussed. The time evolution is discretized for numerical simulation by employing the Suzuki-Trotter approximation. We tested the evolution with several time steps and consequently found that the appropriate time step was 0.01. Consider the single qubit density matrix ρ_0 as:

$$\rho_0 = \frac{1}{2} \begin{bmatrix} 1 & 0 \\ 0 & 1 \end{bmatrix} \quad (\text{S3})$$

Then the N qubit state can be written as $\rho_0^{\otimes N}$. For all the results in Fig. 4 in the main text, the system size has been fixed to $N=4$. In the main text, Fig. 4(a), we present the temporal evolution of the Hamiltonian's expectation value in the presence of non-Markovian errors. The black curve in main text Fig. 4(a) delineates the time evolution of the target Hamiltonian, while the blue curve portrays the system's time evolution, accounting for errors resulting from fluctuations in the coefficients of the Hamiltonian (ω, Δ , and V). All the coefficients for the

target Hamiltonian are set to 1 with added fluctuations, which are drawn randomly from a Gaussian distribution comprising 10,000 samples, each with a central value of 1 and a standard deviation of 0.1. The ultimate expectation value of the Hamiltonian, incorporating errors, is computed by performing a statistical average across all 10,000 samples. If the system is allowed to evolve for an extended time scale, it will be revealed that the expectation value of the Hamiltonian, when affected by errors, would finally converge to the expectation value of the target Hamiltonian. In Fig. 4(b), we add five distinct error offsets, denoted as σ_o , to the Hamiltonian coefficients and illustrate its expectation value of Hamiltonian versus time. Fig. 4(c) shows the maximum deviation of the time-evolved Hamiltonian with the target Hamiltonian for various system sizes. The error for each system size was added in the same way as calculated for Fig 4(b). The inset within Fig. 4(c) presents the expectation value of the maximum difference between the target Hamiltonian and the time-evolved Hamiltonian as a function of the σ_0 values used in Fig. 4(b). In our discussion of Fig. 4 in the main text, it's crucial to mention that we've maintained zero systematic error throughout. This is achieved in the simulation by ensuring that the average value of the Gaussian distribution, which generates fluctuations for the coefficients, matches the actual coefficient we've assigned to the target Hamiltonian.